Modeling of Pore Parameters and Experimental Validation Using the Microstructure of 0.85Mo and 1.5Mo Prealloyed Sintered Steels

Samuel Tesfaye Mekonone[1(✉)], Alberto Molinari[2], and Solomon Mesfin Demlie[3]

[1] Addis Ababa University, Addis Ababa, Ethiopia
samuel.tesfaye@aait.edu.et
[2] University of Trento, Trento, Italy
alberto.molinari@unitn.it
[3] University of Gondar, Gondar, Ethiopia

Abstract. Empirical models were developed to relate stress with a resistance of materials that helps to predict the response of materials. For porous materials, measuring the pore parameters is required to incorporate the intensification effect of the pore on the stress distribution. However, image analysis is the common practice employed to measure pore parameters, mathematical models may also use as an alternative method. Mathematical modeling of pore parameters for square, triangular, and rectangular geometric pore was developed. Pore parameters used to characterize circularity (f_{circle}), elongation (f_{shape}), and the pore size (equivalent diameters, $D_{eq.}$) were analyzed for those geometric pores. The analytical results were compared with the pore parameters measured on the microstructures of prealloyed sintered steels. The modeling results are in agreement with the experimental analysis.

Keywords: Pore parameters · Geometric models · Sintered steels · Microstructures · Image analysis

1 Introduction

Pinions, gears, bearings, and cams are among the mechanical components produced by powder metallurgy. Porosity is the inherent characteristic of the microstructure of these components that are processed by powder compaction and subsequent sintering processes. To evaluate their resistance to mechanical loading, characterization of pore parameters, such as size, distribution, and the shape is required to incorporate its effect on the stress distributions [1–4]. Measuring these parameters on the microstructures using image analysis, that is the direct techniques of quantitative characterization of PM materials, is well adopted and used to understand its effect on the mechanical behaviors [5–8]. Bending and contact fatigue are the major damage mechanisms of PM components that are determined by the presence of porosity in the microstructure [9–11]. Fatigue limit and fatigue life of PM materials are usually lower as compared with the

M. A. Delele et al. (Eds.): ICAST 2020, LNICST 385, pp. 245–260, 2021.
https://doi.org/10.1007/978-3-030-80618-7_16

pore-free materials. The reduction of mechanical properties relates to the decreasing of load bearing surface, and pore acts as a notch effect in the microstructures [12–16]. It is acting as stress or strain intensifying zones [17], and specifically elongated and large pore typically become the site of crack nucleation that reduces the fatigue limit and the material tends to fail at lower stress. The mechanism used to improve the mechanical properties is controlling the compaction and sintering process to reduce the size and volume of porosity and to prepare rounded pore morphology [18]. Therefore, understanding the size and shape of the pore is an important step in the process of PM materials that help to predict its response to the applied loads. Currently, there is a trend to link the size of the bigger pore, pore distribution, and pore shape parameters with mechanical properties (specifically contact fatigue and fatigue strength) [19]. Based on the conservative approach, contact fatigue crack nucleation was predicted by comparing the yield strength of diffusion alloyed PM materials with applied stress where the analysis of stress incorporates notch effect [20].

The derivation of contact stress considers the effect of bigger pores (10% of the pore population corresponds to the total pore population) as stress intensifying area and deteriorate load bearing sections, where the analysis needs a measurement of pore parameters. This research work aims to model pore geometries and evaluate the pore parameters that can be considered as required inputs for the analysis of stress distribution in the porous microstructures. Modeling of the pore with the following geometries was proposed.

1. Square geometric pore (□) – formed between four particles.
2. Triangular geometric pore (△) – formed between three particles.
3. Rectangular geometric pore (▭) – formed between four particles.

Then the model results are validated by comparing with the pore parameters measured using image analysis that was carried out on low alloyed PM steel microstructures. Quantitative characterization of pore shape and size is possible with a lack of precision and universal definition of terms [21]. But the Shape factor parameter such as f_{shape} (characterizes pore elongation), f_{circle} (characterizes pore circularity) is well adapted to characterize the porous microstructures.

2 Pore Modeling, Materials, and Experimental Methods

2.1 Mathematical and Geometric Modeling of Pore

Analytical modeling of pore geometry in porous material was complex due to the diversity of pores shapes, orientations, and sizes. However, a limited number research papers have reported the pore parameters analyzed based on atomistic and macroscopic modeling approaches of compaction and sintering of PM materials [22–25] According to the classical model, a sharp neck is created between two perfect spherical particles (represents the initial stage of the sintering), and from the geometry, the ratio of neck to particle size is related by $X/D > 0.3$, where X is neck size and D is the particle size [5]. But no relationship was developed between neck and particle size at the final stage of sintering (decreased in size and became rounded), however, it became a critical parameter that can

determine the behavior of the final product, only limited analytical and numerical model available for the final stage of sintering. On the one hand, because of several geometries of pore evolution and on the other hand, this is influenced by compaction/sintering parameters. This results in the complex geometry of pore and microstructural evolutions which is not the easy task to study analytically or numerically. However, there is a strong relation between pore parameters of sintered microstructure and green body compaction pressure [5], neck formation between grains affected manly by sintering temperature, and time that can be incorporated in these work. The relationship between R′ (refers to neck size) and R/r (refers to particle size) of the simple geometry and compared with the results of image analysis on the microstructure. The influence of the compaction/sintering parameter is not considered here in the models. Figure 1 illustrates the proposed pore models that are defined by the spaces between spherical particles.

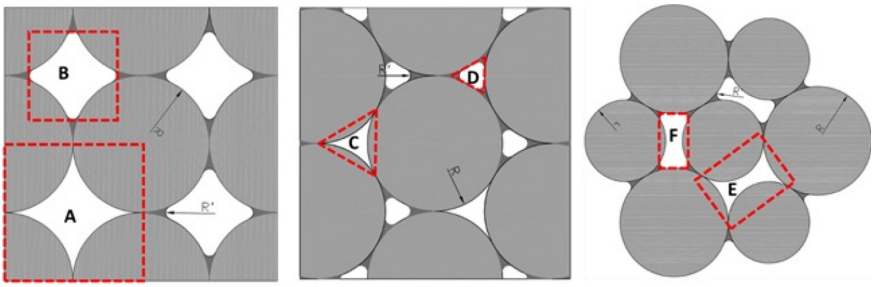

Fig. 1. The three types of pore models: square (A, B), triangular (C, D) and rectangular (E, F) geometric pores

The pore geometries, highlighted in the red in Fig. 1, are voids that are defined based on the number of contacts between spherical grains and grain size. These six pore geometries are characterized as follows:

- A and B are square geometric pores formed between four equal particles (it radius is R) with sharp ($R' = 0$) and rounded ($R' > 0$) edge, respectively;
- C and D are triangular pores formed between three equal particles (it radius is R) with sharp ($R' = 0$) and rounded ($R' > 0$) edge, respectively;
- E and F are rectangular geometric pores formed between different sized particles (its radius are R and r) with sharp ($R' = 0$) and rounded ($R' > 0$) edge, respectively.

Mathematical models are required to correlate the grain size and number of contacts with the proposed pore models that aim to analyzed and characterized the pore parameters. Three pore models as a square, triangular and rectangular geometries were defined in both cases of sharp and rounded edges. A sharp-edged pore model is, which is the simplest one, formed when the particles undergo a point contact, or the radius (R') of the rounded edge is zero, and the size and shape of the three pore models vary with R and R'. The modes can be defined based on those dimensions except for rectangular geometries formed between particles with different sizes (R and r), which requires an additional characteristic that is the gap between particles of similar sizes. Besides, the

morphology of these pore models is irregular in shape and with a certain error, it can be used to represent the voids in the microstructures of PM materials. The pore parameters (f_{circle} and f_{shape}) are always less than 1 unless otherwise, all pore are perfect circles, which is not mostly realistic in PM microstructures. Circular pore morphology is the desired microstructures of PM materials because it provides good mechanical properties than irregular pores [11] and hence not considered here.

Figure 2 represents the pore geometries between three and four particles with triangles to formulate the area of the pore. Triangles were constructed by connecting the center of two particles and one of the rounded neck. α and β are angles of these triangles. The maximum and minimum diameter of the pore are highlighted as red and blue colors in the figure. The maximum diameter is the largest distance between two parallel lines, which passes through the edges or lines of pore without crossing the area of the pore. The minimum diameter is the smallest distance between two parallel lines, which passes through edges or lines of pore without crossing the area of the pore.

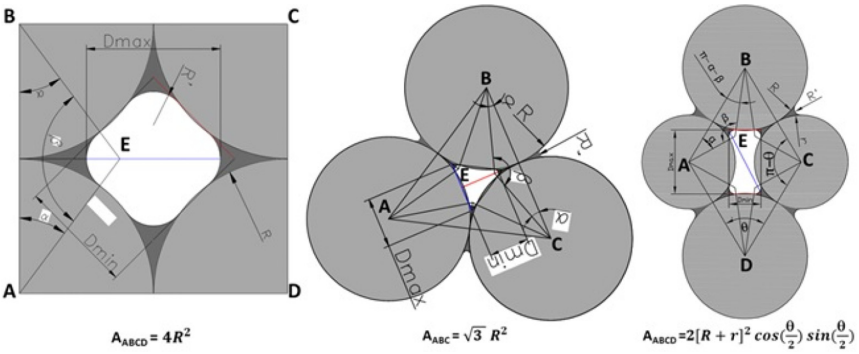

Fig. 2. Geometrical relation of pores and circumscribed geometries

Square (ABCD), equilateral triangle (ABC), and rhombus(ABCD) circumscribe a square, triangle, and rectangular geometric pore models. The side length of a square (ABCD) and triangle (ABC) is 2R and the rhombus has R + r equal side lengths and the area of three geometries are $4R^2$, $\sqrt{3}R^2$ and $2[R + r]^2 \cos\left(\frac{\theta}{2}\right) \sin\left(\frac{\theta}{2}\right)$. These parameters use to drive for pore areas.

The area of the square geometric pore ($R' = 0$) valuated by subtracting the area of four circular sectors (characterized by the radius R and angle 90°) from an area of square ABCD. Area of the square geometric pore with the sharp neck ($A_{sharp\ neck,\ \square}$) is given by Eq. (1).

$$A_{sharp\ neck,\ \square} = (4 - \pi)R^2 \tag{1}$$

Area of the triangular geometric pore with the sharp neck ($A_{sharp\ neck,\ \triangle}$) evaluated by subtracting the area of three circular sectors (characterized by the radius R and angle 60°) from an area of a bigger equilateral triangle ABC and is given by Eq. (2).

$$A_{sharp\ neck,\ \triangle} = \left(\sqrt{3} - \frac{\pi}{2}\right)R^2 \tag{2}$$

Area of the rectangular geometric pore with the sharp neck ($A_{\text{sharp neck, }\square}$) evaluated by subtracting the area of four circular sectors (characterized by the radius R/r and angles $\theta/\pi - \theta$) from an area of rhombus ABCD is given by Eq. (3).

$$A_{sharp\ neck,\ \square} = 2(R+r)^2 cos\left(\frac{''}{2}\right) sin\left(\frac{\theta}{2}\right) - r^2(\pi - \theta) - R^2\theta \tag{3}$$

Figure 3 illustrates the triangles ABE constructed from the square, triangular, and rectangular geometric pore. with a side length of R + r, r + R′, and R + R′. When the particle size is the same such as, R = r, square and rectangular geometric pore is the same. A_3 (grown neck area between particles) should be excluded from the rounded neck pore model by subtracting from the area of sharp neck pore.

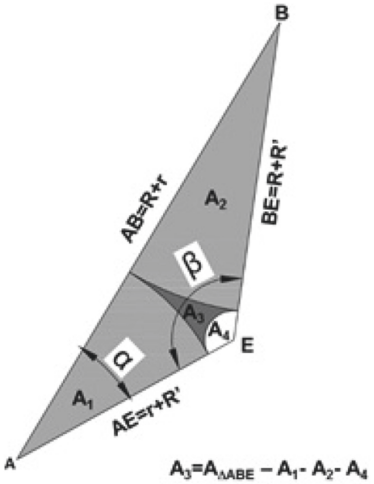

Fig. 3. Triangle ABE and its vertices are at the centers of particles and neck curvature

The pore geometries and dimensions mathematically correlated with the particle and neck size using Heron's formula and cosine rules. The angles of triangle ABE calculated from Eq. (4) and Eq. (5) (cosine rule).

$$cos\alpha = \frac{AE^2 + AB^2 - BE^2}{2AE * AB} \tag{4}$$

$$\cos\beta = \frac{AE^2 + BE^2 - AB^2}{2AE * BE} \tag{5}$$

Area of triangle (A_{ABE}) is given by Eq. (6) (Heron's formula).

$$A_{\triangle ABE} = \sqrt{P(P-AB)(P-AE)(P-BE)} \tag{6}$$

Where P is the semi perimeter of the triangle and it is given by $P = 2R + R'$ for square and triangular pore and $P = R + r + R'$ for rectangular pore model.

A_3 (as described by Fig. 3) was evaluated using Eq. (7).

$$A_3 = \begin{cases} R\sqrt{2RR' + R'^2} - \frac{R'^2(\pi - 2\alpha)}{2} - R^2\alpha, & square\ or\ triangular\ pore \\ \sqrt{RrR'(R + r + R')} - \frac{R^2(\pi - \alpha - \beta)}{2} - \frac{R'^2}{2} - \frac{r^2\alpha}{2}, & Rectangular\ pore \end{cases} \quad (7)$$

Therefore, the area of square/rectangular pore with rounded neck ($A_{\text{round neck, }\square}$) can be evaluated by subtracting 4 times of A_3 from the total area of the pore with a sharp neck (Eq. (2)) and is given by Eq. (8).

$$A_{\text{round neck, }\square} = A_{\text{sharp neck, }\square} - 4 * A_3 \quad (8)$$

Similarly, the area of triangular pore between three particles with round neck ($A_{\text{round neck, }\triangle}$) is given by Eq. (9).

$$A_{round\ neck,\ \triangle} = A_{sharp\ neck,\ \triangle} - 3 * A_3 \quad (9)$$

Perimeter is an important parameter of geometries used to quantify the morphological parameters of a pore. It is defined as the total length or circumference of the pore. For the pore with a sharp neck (square and rectangular), the total perimeter is the sum of the arc length of four sectors (with radius R/r) shared by the pore area. And similarly, the perimeter of a triangular pore is the sum of the three arc length of sectors (the radius R and angle 60°). The perimeter of the pore with a rounded neck is determined by subtracting the perimeter of a shaded area (A_3) from the perimeter of the pore with a sharp neck. The perimeter and area of the three geometric pore models are reported in Table 1.

Table 1. Perimeter and area of a square, triangular and rectangular pore models

Pore model	pore perimeter, P	pore area, A
Square	$\begin{cases} 2\pi R, & R' = 0, \\ 4\left(\frac{\pi}{2} - 2\alpha\right)R + 4(\pi - 2\alpha)R', & R' < 0 \end{cases}$	$\begin{cases} (4 - \pi)R^2, & R' = 0, \\ (4 - \pi)R^2 - 4\left\{R\sqrt{2RR' + R'^2} - \frac{R'^2(\pi - 2\alpha)}{2} - R^2\alpha\right\}, & R' > 0 \end{cases}$
Triangular	$\begin{cases} \pi R, & R' = 0, \\ 3\left(\frac{\pi}{3} - 2\alpha\right)R + 3(\pi - 2\alpha)R', & R' < 0 \end{cases}$	$\begin{cases} \left(\sqrt{3} - \frac{\pi}{2}\right)R^2, & R' = 0, \\ \left(\sqrt{3} - \frac{\pi}{2}\right)R^2 - 3\left\{R\sqrt{2RR' + R'^2} - \frac{R'^2(\pi - 2\alpha)}{2} - R^2\alpha\right\}, & R' > 0 \end{cases}$
Rectangular	$\begin{cases} 2R + 2r(\pi -), & R' = 0, \\ 2R + 2r(\pi -) - 4r\alpha - 4R(\pi - \alpha - \beta) + 4R'\beta, & R' < 0 \end{cases}$	$\begin{cases} 2(R + r)^2 \cos\left(\frac{\theta}{2}\right)\sin\left(\frac{\theta}{2}\right) - r^2(\pi -) - R^2, & R' = 0, \\ 2(R + r)^2 \cos\left(\frac{\theta}{2}\right)\sin\left(\frac{\theta}{2}\right) - r^2(\pi -) - R^2 - 4\left\{\sqrt{RrR'(R + r + R')} - \frac{R^2(\pi - \alpha - \beta)}{2} - \frac{r^2\alpha}{2} - \frac{R'^2\beta}{2}\right\}, & R' > 0 \end{cases}$

The equivalent diameter of the pore model is given by Eq. (10).

$$D_{eq.} = 2\sqrt{\frac{A}{\pi}} \quad (10)$$

Where A, is the pore area (reported in Table 1).

f_{shape} is defined by Eq. (11).

$$f_{shape} = \frac{D_{min}}{D_{max}} \tag{11}$$

Where, D_{max} and D_{min}, are maximum and minimum diameters of the pore, highlighted as blue and red colors in Fig. 4 and Fig. 5. The maximum and minimum diameters of square and rectangular geometric pore between four particles are given by Eq. (12) and Eq. (13), which is derived from the detailed geometry as illustrated in Fig. 4.

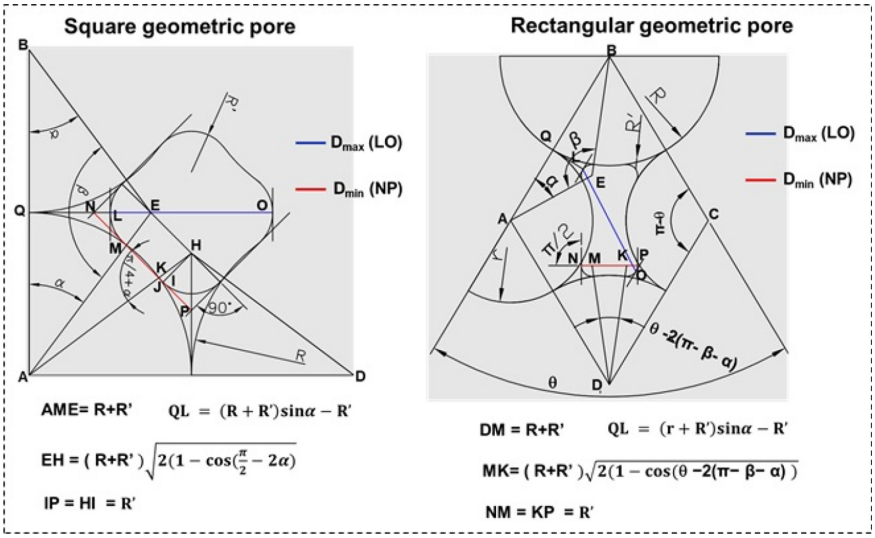

Fig. 4. Detail geometry of the square and rectangular geometric pore models

$$D_{min} = \begin{cases} 2IP + EH = 2R' + [R + R']\sqrt{2(1 - \cos\left(\frac{\pi}{2} - 2\alpha\right)}\text{, for } \square \text{ model} \\ 2KP + MK = 2R' + [R + R']\sqrt{2(1 - \cos(\theta - 2(\pi - \beta - \alpha)}\text{, for } \square \end{cases} \tag{12}$$

$$D_{max} = \begin{cases} AD - 2QL = 2[R + R'](1 - sin\alpha), \text{ for } \square\ model \\ AD - 2QL = (R + R') + [r + R'](1 - 2sin\alpha)\text{, for } \square \text{model} \end{cases} \tag{13}$$

The minimum and maximum diameters of the triangular geometry pore is given by Eq. (14) and Eq. (15), which is derived from the detailed geometry as illustrated in Fig. 5.

$$D_{min} = D_{max}\sin\left(\frac{\pi}{3}\right) - IJ = D_{max}\sin\left(\frac{\pi}{3}\right) - R'\left[\sqrt{\tan^2\left(\frac{\pi}{3} - 2\alpha\right)} - 1\right] \tag{14}$$

$$D_{max} = 2NJ + FG = 2R'\tan\left(\frac{\pi}{3} - 2\alpha\right) + [R + R']\sqrt{2(1 - cos\left(\frac{\pi}{3} - 2\alpha\right)} \tag{15}$$

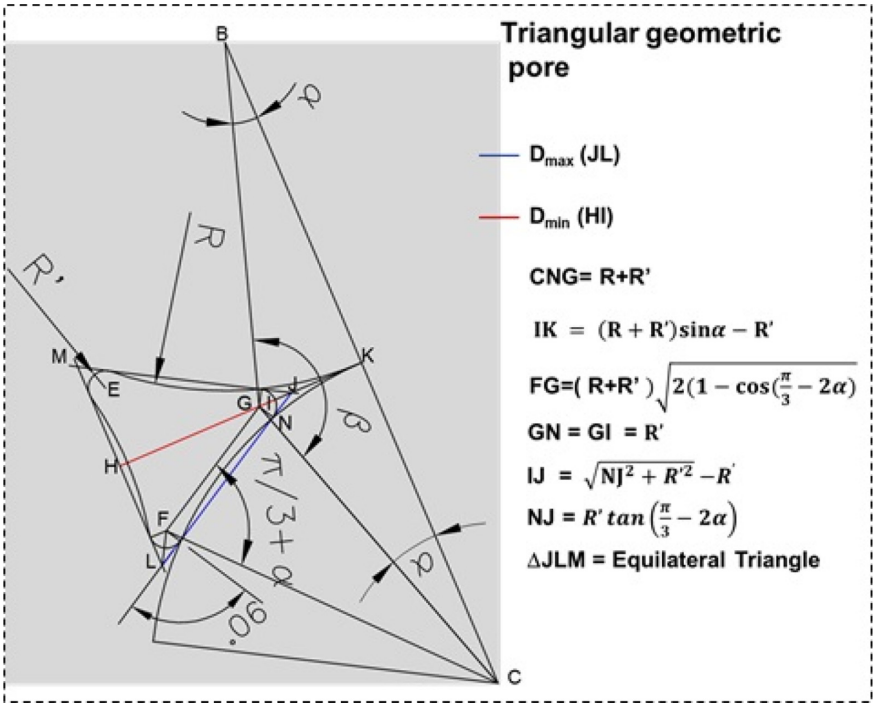

Fig. 5. Detail geometry of triangular pore

An additional characteristic of pore parameters is the circularity of pore. It is defined by Eq. (16).

$$f_{circle} = \frac{4\pi A}{P^2} \tag{16}$$

where A and P are the area and perimeter of pore models (reported in Table 1).

2.2 Materials and Experimental Methods

Two different Fe-Mo-C (interims of different Mo compositions) low prealloyed PM materials were used to study the pore characteristics. These powders compacted in double-action compaction then green compacts, which are rings, sintered at 1150 °C for 30 min, and maintained its final dimensions of 16 × 40 × 10 mm (inner diameter, outer diameter, and height, respectively). Density measurement was performed by the water displacement (WD) using a weighing balance accuracy of 0.0001 g and also calculated from the results of image analysis (IA) on the microstructures. Before microstructure preparation, the specimens were cleaned properly using toluene in the microwave, mounted in risen and gently ground from 220 to 1200.gride silica carbide polishing paper, and then polished using 3 and 1 μm alumina paste/slurry. For Image analysis, an optical microscope was used to prepare micrograph images on unattached spacemen. Seven images were taken on the contact surface (from 0–400 μm depth) of

each material. To avoid the potential effect of shape parameter variation due to magnification over the microstructure, 20× magnification was selected [13]. Porosity, equivalent diameter, perimeter, aspect ratio, breadth, and length of pore were measured, and then f_{circle}, f_{shape} were calculated.

3 Results and Discussion

In this section, pore size between grains, elongation, and circularity was discussed based on the analysis of the theoretical models developed using the relationship of grain sizes, number of grain contacts, and pore geometry. Again, these pore parameters were measured using image analysis applied on the microstructures of sintered steels that were used to validate the theoretical results. Figure 6 illustrates the correlation between the diameter of grain (2R) and the equivalent diameter ($D_{eq.}$) of the pore.

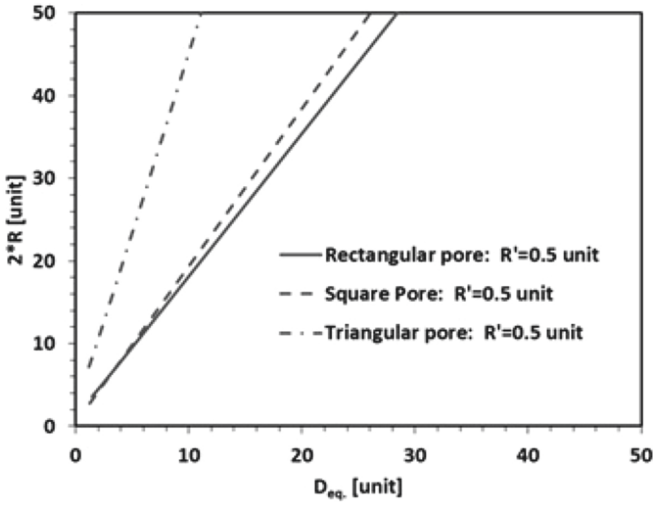

Fig. 6. Equivalent diameter versus particle size of square, triangular and rectangular pore models

The Equivalent diameter of rectangular, square, and triangular pore models varies linearly with the grain size. For a given grain diameter, the equivalent diameter of the triangular pore model is smaller than square and rectangular pore models. This variation shows that the triangular geometric pore may be suited to model only pores with smaller in sizes, while rectangular and square pore models are used for the bigger pores.

The circularity and shape of the pore models using triangular, rectangular, circular geometries were analyzed, and Fig. 7 represents f_{circle} of the three pore models.

The area of rectangular, square, and triangular pore models is made to vary with the distance between grains (H) which is a function of the grain (R) and neck sizes (R′). Therefore, f_{circle} of the triangular, rectangular, and square pore geometries is a function of the equivalent diameter that is dependent on grain (R) and neck (R/r nad R′) sizes too. For the three models and sharp neck ($R' = 0$), f_{circle} is constant and independent of the

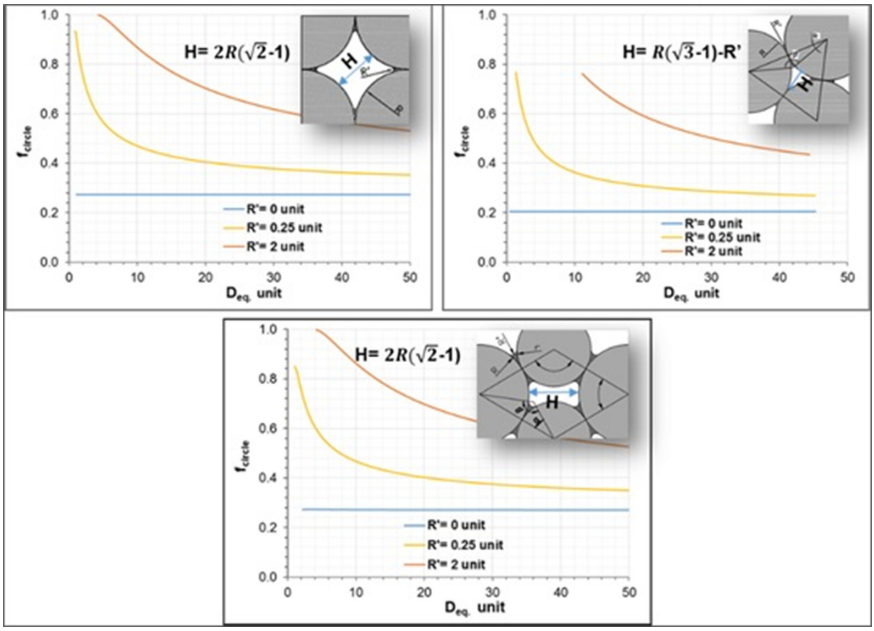

Fig. 7. Equivalent diameter versus f_{circle} of square, triangular and rectangular pore models

pore size. The circularity of square/rectangular and triangular pore models with sharp corners is 0.21 and 0.27, respectively, that is the bottom line to the value of f_{circle}. When neck size increases (from 0 to 2 unit), f_{circle} also increases that attributes to the formation of a rounded pore shape as the size of the length of the curved neck increases. But, at a constant neck size, circularity decreases with an increasing equivalent diameter of pore models. Pores with smaller equivalent diameter are characterized by higher circularity, and a perfect circular pore has $f_{circle} = 1$. However, the pore becomes elongated and its circularity decreases as equivalent diameter increases.

Figure 8 illustrates the relationship of $D_{eq.}$ and f_{shape} of triangular, rectangular, and square pore models.

The horizontal bottom line indicates that the constant f_{sahpe} of the pore with a sharp edge ($R' = 0$) and the values are 0.71, 071, and 0.87 for rectangular, square, and triangular pore models, respectively. f_{shape} of the rectangular and square pore model is lower than the triangular pore model at the equal equivalent diameter and neck size. A similar trend was observed for f_{circl} and f_{shape} and both decreases with increasing equivalent pore size. Pores with smaller equivalent diameters are characterized by lower in irregularity and equivalent with a rounded geometry that results in a higher f_{shape}, then it equated to 1 as the geometry approaches a circular pore.

Again, the relationship between pore shape and circularity was analyzed, and Fig. 9 represents f_{circle} versus f_{shape} of triangular, rectangular, and square pore models with a variable gap between contacted grains and fixed height between bigger particles.

Since contacting grains that are used in the molding of the square and triangular pores are equal in size, the gap between grains (H) increases linearly with the grain size

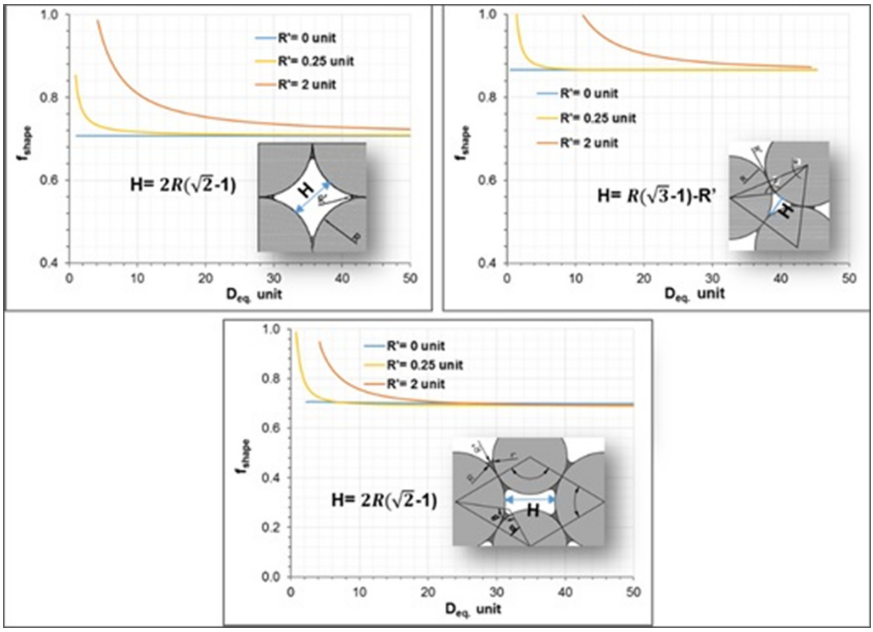

Fig. 8. Equivalent diameter versus f_{shape} of square, triangular and rectangular pore models

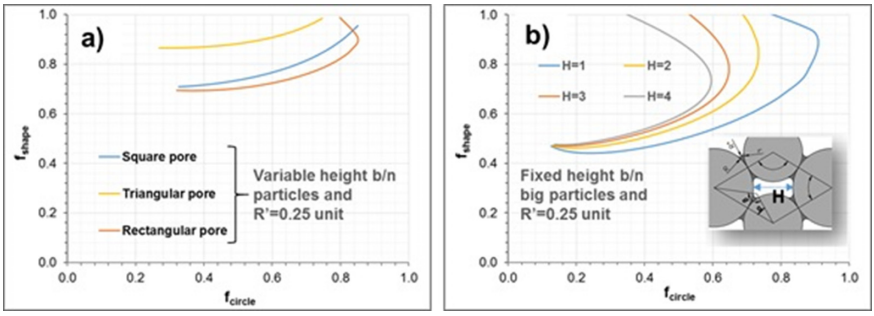

Fig. 9. f_{circle} versus f_{shape} of the three pore models: a) at a gap between grains (defined by, $H = 2R\left(\sqrt{2}-1\right)$ for rectangular and square models, and $H = R\left(\sqrt{3}-1\right) - R'$ for triangular pore), and b) at a different fixed height between bigger grains of the rectangular model.

(R), and it does not affect the relationship between f_{circle} and f_{shape}. However, for the rectangular pore model, the size of the grains is not the same (characterized using R and r), such that the gap between grains depends on the size of the grain. At a fixed distance between larger grains, and as the gap between smaller particles is increasing, the relationship between f_{circle} and f_{shape} can be variable. Therefore, the relationship of circularity and elongation for the square, triangular and rectangular pore models shows similar trends of variations, and for rectangular pore geometry, the gap between particles is the determinate factor to f_{circle} and f_{shape} relation.

To validate these theoretical results, first density and total porosity of Fe-0.85%Mo-0.35%C and Fe-1.5%Mo-0.3%C sintered steels were characterized using water displacement methods and image analysis techniques, respectively. Again, the image analysis data were elaborated to determine the pore parameters (equivalent diameter, circularity, elongation). The density and porosity of the two PM steels are reported in using Table 2.

Table 2. Density and porosity of prealloyed PM steels

Material	Porosity, ε	Density, g/cm3
0.85%Mo steel	0.06 ± 0.01	7.33 ± 0.04
1.5%Mo steel	0.05 ± 0.01	7.41 ± 0.04

Again, the density and porosity of the two materials were determined from the microstructures. Figure 10 shows the microstructures of carburized and heat treated 0.85%Mo and 1.5%Mo prealloyed PM steel at the surface that were prepared after sectioning of the cylindrical specimen longitudinally.

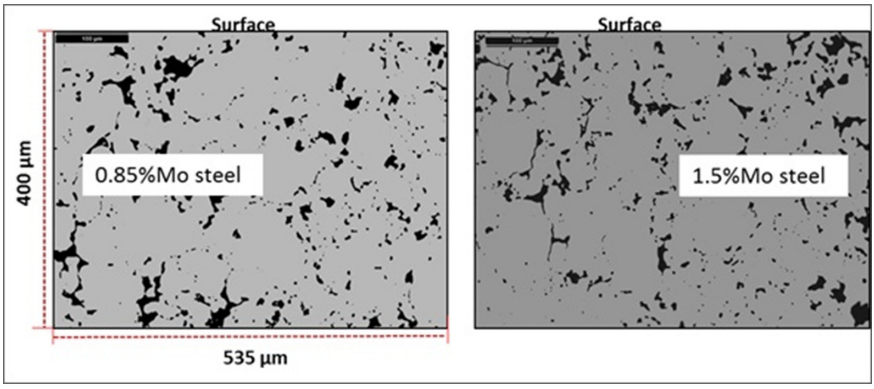

Fig. 10. Microstructure at the surface of carburized and heat treated low alloyed steels

To measure the pore parameters, image analysis was carried out on the surfaces of seven adjacent microstructures (each has a total area of 400 × 535 µm) on each PM steels. The average porosity and pore parameters were collected within 50 µm range up to the total depth of 400 µm. Average porosity 0.85% Mo and 1.5% Mo steels are 0.07 ± 0.01 and 0.07 ± 0.02, respectively.

Figure 11 represents f_{circle} and f_{shape} corresponding to 100% of pore populations measured by image analysis and three geometric pore models.

The results of pore models and image analysis shows that f_{circle} decreases with increasing equivalent pore diameters. However, f_{shape} determined from the model relatively higher than determined from the experimental results of the two materials. Image

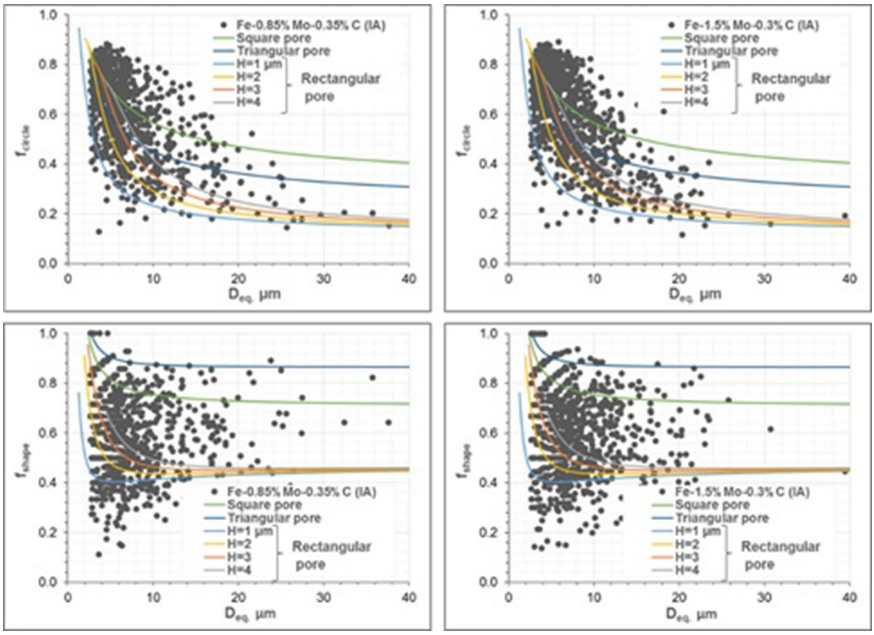

Fig. 11. f_{circle} and f_{shape} of the three pore model and image analysis of the micrograph 270 μm width by 400 μm depth.

analysis results of the irregular pore with lower circularity and shape are well fitted with a rectangular geometric pore model, whereas the pore with higher circularity and shape are well fitted with the square and triangular pore models. However, the pore morphology and sizes are statistical and the experimental results may not be expected to fit exactly with the model results, however, the results of f_{circle} and f_{shape} determined based on the two approaches are still comparable. Moreover, the rectangular pore model is agreed more with the smaller and larger size pore populations, and the square and triangular pore model agreed more with the smaller size and rounded pore populations. The large pore with rounded in morphology (large R and R′, as it is illustrated using Fig. 7) of the pore model, may greatly approximate to explain the circularity of the pore characterized by image analysis. Therefore, the neck size, R′, can be an important parameter of the pore modeling, which can be liked with sintering parameters. To model, the pore in the microstructure of PM materials depends on different processing parameters such that, R′ can vary from zero to certain values. It is merely related to the type of materials and microstructures. Therefore, using larger R′ may get higher priority and could get good agreement with a material having a larger pore size and rounded morphology. R′ = 0.25 μm found to be the best fit with the microstructures of 0.85%Mo and 1.5%Mo steels.

f_{shape} collected from the microstructures is more elongated in shape. On the contrary, the model shows rounded pore, f_{shape} values are above 0.87 and 0.701 for triangular and square pore models, respectively. This indicates that the pore is not elongated as it is

observed from the microstructures. But the small R′ can be selected to fit with the data from image analysis of densified and rounded porous materials.

Figure 12 represents the comparisons of results of f_{circle} versus f_{shape} analyzed from the theoretical models and image analysis of the microstructures of the two PM steels.

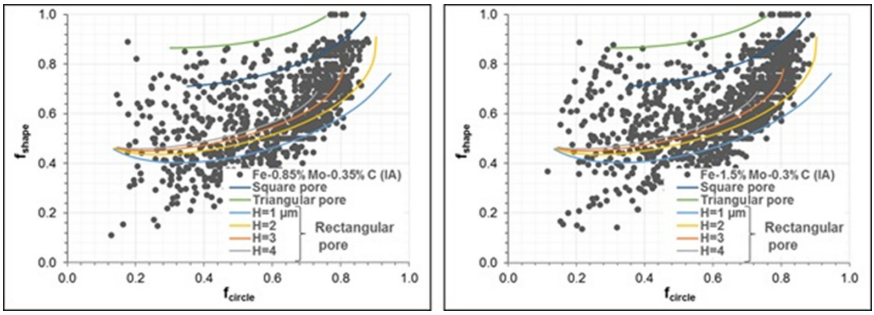

Fig. 12. f_{circle} versus f_{shape} of three geometric pore model and image analysis.

The experimental results show that a similar trend of variation between f_{circle} and f_{shape} was observed as it determined from the square, triangular, and rectangular pore models. The smaller pore size, which is characterized as rounded and regular pore, can be represented using square and triangular pore models, whereas the bigger pore, which is characterized as more irregular pore, can be represented using a rectangular pore model. Besides, a rectangular pore model with a neck size of $R' = 0.25\ \mu m$ is comparable with the data of image analysis.

4 Conclusions

The theoretical model to characterize equivalent diameter, circularity, and elongation of pores between the contacts of three and four grains with sharp and rounded necks were analyzed. Based on the number of contacts between grains, grain size, and neck size, a mathematical model was formulated to determine the equivalent diameter and pore parameters (f_{shape} and f_{circle}) of the pore formed between grains. To validate the model results, image analysis was carried out to measure porosity, equivalent pore diameter, pore area, and perimeter on the microstructure of Fe-0.85%Mo-0.35%C and Fe-1.5%Mo-0.3%C prealloyed PM material that used to analyze the pore parameters. The model is comparable with image analysis results and the following conclusion is drawn from the results,

- A pore model with a sharp neck is used to determine the lower limit of circularity (f_{circle}) and elongation (f_{shape}).
- The Square and triangular pore models represent the pore with higher circularity. But the rectangular geometric pore model is exactly fitted with irregular and larger pore size.

- Modeling of the pore parameters of a pore with a rounded neck shows better agreement with the results of image analysis, in particular, f_{circle} and f_{shape} of pore populations with smaller pore fits well with square and triangular pore models. Whereas the rectangular geometric pore model is well fitted with pore populations with irregular and larger pore size.
- As future work, the model is important to link the effect of pore size, shape, and morphology with the mechanical properties. In particular, nucleation of fatigue and contact fatigue cracks can be the prominent areas.

References

1. Cristofolini, I., Molinari, A., Straffelini, G., Muterlle, P.V.: A systematic approach to design against wear for powder metallurgy (PM) steel parts: the case of dry rolling-sliding wear. Mater. Des. **32**(4), 2191–2198 (2011)
2. Metinöz, I., Cristofolini, I., Pahl, W., DeNicolo, A., Marconi, P., Molinari, A.: Theoretical and experimental study of the contact fatigue behavior of a Mo–Cu steel produced by powder metallurgy. Mater. Sci. Eng. A **614**, 81–87 (2014)
3. Mekonone, S.T., Pahl, W., Molinari, A.: Influence of the microstructure on the subsurface and surface damage during lubricated rolling-sliding wear of sintered and sinterhardened 1.5%Mo–2%Cu–0.6%C steel: theoretical analysis and experimental investigation. Powder Metall. **61**(3), 187–196 (2018)
4. Tesfaye, S., Molinari, A., Pahl, W.: Damage phenomena in lubricated rolling-sliding wear of a gas carburised 0.85%Mo low-alloyed sintered steel: theoretical analysis and experimental verification. Powder Metall. 1–9 (2017)
5. German, R.M.: Sintering Theory and Practice (1996)
6. German, R.M.: Powder Metallurgy Science, Met. Powder Ind. Fed. 105 Coll. Rd E Princet. N J 08540 U 1984 279 (1984)
7. German, R.M.: Powder Metallurgy of Iron and Steel. John Wiley Sons Inc 605 Third Ave N. Y. NY 10016 USA 1998 496 (1998)
8. Tomić, N.Z., et al.: Image analysis and the finite element method in the characterization of the influence of porosity parameters on the mechanical properties of porous EVA/PMMA polymer blends. Mech. Mater. **129**, 1–14 (2019)
9. Sonsino, C.M.: Fatigue design for powder metallurgy. Met. Powder Rep. **45**(11), 754–764 (1990)
10. Sonsino, C.M.: Fatigue design principles for sintered steel components. J. Strain Anal. Eng. Des. **41**(7), 497–555 (2006)
11. Benedetti, M., Menapace, C.: Tooth root bending fatigue strength of small-module sinter-hardened spur gears. Powder Metall. **60**(2), 149–156 (2017)
12. EUDIER, M. : The mechanical properties of sintered low-alloy steels. Powder Metall. **5**(9), 278–290 (1962)
13. Fleck, N.A., Smith, R.A.: Use of simple models to estimate effect of density on fracture behaviour of sintered steel. Powder Metall. **24**(3), 126–130 (1981)
14. Williams, S.H., Haynes, R.: Effect of porosity on the fatigue behaviour of sintered precipitated nickel powder. Powder Metall. **16**(32), 387–404 (1973)
15. Fleck, N.A., Smith, R.A.: Effect of density on tensile strength, fracture toughness, and fatigue crack propagation behaviour of sintered steel. Powder Metall. **24**(3), 121–125 (1981)
16. Hanejko, F., Rawlings, A., Narasimhan, K.S.V.: Surface densified P/M steel–comparison with wrought steel grades. In: Euro PM2005 Prague, pp. 509–511 (2005)

17. Chawla, N., Deng, X.: Microstructure and mechanical behavior of porous sintered steels. Mater. Sci. Eng. A **390**(1), 98–112 (2005)
18. Kubicki, B.: Stress concentration at pores in sintered materials. Powder Metall. **38**(4), 295–298 (1995)
19. Andersson, M.: The role of porosity in fatigue of PM materials. Powder Metall. Prog. **1**, 11 (2011)
20. Molinari, A., Metinöz, I., Cristofolini, I.: A conservative approach to predict the contact fatigue behavior of sintered steels. Powder Metall. Prog. **1**, 7 (2014)
21. Martin, W.D., Putman, B.J., Kaye, N.B.: Using image analysis to measure the porosity distribution of a porous pavement. Constr. Build. Mater. **48**, 210–217 (2013)
22. Brewin, P.R., Coube, O., Doremus, P., Tweed, J.H. (eds.): Modelling of Powder Die Compaction. Springer-Verlag, London (2008)
23. Samal, P., Newkirk, J. (eds.): Modeling and simulation of press and sinter powder metallurgy [1]. In: Powder Metallurgy. ASM International, pp. 179–190 (2015)
24. Rojek, J., Nosewicz, S., Maździarz, M., Kowalczyk, P., Wawrzyk, K., Lumelskyj, D.: Modeling of a sintering process at various scales. Proc. Eng. **177**, 263–270 (2017)
25. Pan, J.: Modelling sintering at different length scales. Int. Mater. Rev. **48**(2), 69–85 (2003)